



Minerva Access is the Institutional Repository of The University of Melbourne

Author/s:

Kohn, B;Weissbrod, T;Chung, L;Farley, K;Bodorkos, S

Title:

Low-temperature thermochronology of francolite: Insights into timing of Dead Sea Transform motion

Date:

2019-06-01

Citation:

Kohn, B., Weissbrod, T., Chung, L., Farley, K. & Bodorkos, S. (2019). Low-temperature thermochronology of francolite: Insights into timing of Dead Sea Transform motion. *Terra Nova*, 31 (3), pp.205-219. <https://doi.org/10.1111/ter.12387>.

Persistent Link:

<https://hdl.handle.net/11343/285699>

1  
2  
3  
4  
5  
6  
7  
8  
9  
10  
11  
12  
13  
14  
15  
16  
17  
18  
19  
20  
21  
22  
23  
24  
25  
26  
27  
28  
29  
30  
31  
32  
33  
34  
35  
36  
37

PROFESSOR BARRY KOHN (Orcid ID : 0000-0001-5064-5454)

Article type : Special issue - Thermo2018

Received date: 14-Nov-2018

Revised version received date: 30-Jan-2019

Accepted date: 28-Feb-2019

Correspondence to:

Professor Barry Kohn

## *Special issue - Thermo2018*

*Title:* Low-temperature thermochronology of francolite: Insights into timing of Dead Sea Transform motion

*Short Title:* Francolite thermochronology - Dead Sea Transform motion

**Barry Kohn<sup>1</sup>, Tuvia Weissbrod<sup>2</sup>, Ling Chung<sup>3</sup>, Ken Farley<sup>4</sup>, Simon Bodorkos<sup>5</sup>**

<sup>1</sup> Address: School of Earth Sciences, University of Melbourne, Victoria, Australia 3010

email: [b.kohn@unimelb.edu.au](mailto:b.kohn@unimelb.edu.au)

phone: +61 3 8344 7217

fax: +61 383 447 761

ORCID: 0000-0001-5064-5454

<sup>2</sup> Address: The Geological Survey of Israel, Jerusalem 95501, Israel

email: [tuviaweissbrod@hotmail.com](mailto:tuviaweissbrod@hotmail.com)

phone: +972 2 6423 104

fax:

ORCID:

<sup>3</sup> Address: School of Earth Sciences, University of Melbourne, Victoria, Australia 3010

**This is the author manuscript accepted for publication and has undergone full peer review but has not been through the copyediting, typesetting, pagination and proofreading process, which may lead to differences between this version and the [Version of Record](#). Please cite this article as [doi: 10.1111/TER.12387](https://doi.org/10.1111/TER.12387)**

This article is protected by copyright. All rights reserved

38 email: lchung1@unimelb.edu.au  
39 phone: +61 3 8344 9669  
40 fax: +61 383 447 761  
41 ORCID:  
42

43 <sup>4</sup>Address: Division of Geological and Planetary Sciences, California Institute of Technology, CA 91125, USA  
44 email: farley@gps.caltech.edu  
45 phone: +1 626 395 6005  
46 fax: +1 626 395 0935  
47 ORCID: 0000-0002-7846-7546  
48

49 <sup>5</sup>Address: Geoscience Australia, Canberra, ACT 2601, Australia  
50 email: Simon.Bodorkos@ga.gov.au  
51 phone: +61 262 495 869  
52 fax: +61 262 499 111  
53 ORCID: 0000-0001-8605-0276  
54

55 This paper was presented at the 16th International Conference on Thermochronology  
56 (Quedlinburg, Germany, September 2018)  
57  
58

## 59 ABSTRACT

60  
61 Cambrian siliciclastic sequences along the Dead Sea Transform (DST) margin in southern  
62 Israel and southern Jordan host both detrital fluorapatite [D-apatite] and U-rich authigenic  
63 carbonate-fluorapatite (francolite) [A-apatite]. D-apatite and underlying Neoproterozoic  
64 basement apatite yield fission track (FT) data reflecting Paleozoic-Mesozoic sedimentary  
65 cycles and epeirogenic events, and dispersed (U-Th-Sm)/He (AHe) ages. A-apatite, which  
66 may partially or completely replace D-apatite, yields an early Miocene FT age suggesting  
67 formation by fracturing, hydrothermal fluid ascent and intra-strata recrystallisation, linked to  
68 early DST motion. The DST, separating the African and Arabian plates, records ~105 km of  
69 sinistral strike-slip displacement, but became more transtensional post-5 Ma. Helium  
70 diffusion measurements on A-apatite are consistent with thermally activated volume  
71 diffusion, indicating  $T_c \sim 52\text{-}56 \pm 10^\circ\text{C}$  (cooling rate  $10^\circ\text{C}/\text{Myr}$ ). A-apatite AHe data record  
72 Pliocene cooling ( $\sim 35\text{-}40^\circ\text{C}$ ) during the transtensional phase of movement. This suggests that  
73 timing of important milestones in DST motion can be discerned using A-apatite low-  
74 temperature thermochronology data alone.

75

## 76 1 INTRODUCTION

77

78 Authigenic apatite (francolite or carbonate-fluorapatite) (A-apatite) has been reported from  
79 Cambrian strata from areas neighbouring the DST in southern Israel, Jordan and Sinai (e.g.  
80 Weissbrod, 1980; Weissbrod & Nachmias, 1986). A-apatite, which may form euhedral  
81 overgrowths on detrital apatite (D-apatite) (e.g. Fig. 6 in Vermeesch et al., 2009), is clearly  
82 post-depositional, yet the age of authigenesis remains unclear. A late Devonian-early  
83 Carboniferous thermal event in southern Israel, and Egypt (Sinai and Eastern Desert) is  
84 recorded in zircon fission track data (Kohn et al., 1992; Bojar et al., 2002; Vermeesch et al.,  
85 2009) and geochronological data from other mineral systems in southern Israel (e.g. Segev et  
86 al., 1995, Heimann et al., 1995, Golan et al., 2018). A-apatites do not appear in strata younger  
87 than Devonian (Weissbrod & Nachmias, 1986), so Vermeesch et al. (2009) and Weissbrod et  
88 al. (1987) proposed that its growth resulted from a pulse of U-rich hydrothermal fluid  
89 circulation related to the Paleozoic thermal event. On the other hand, Segev (1992) suggested a  
90 Neogene age for abundant U-mineralisation and A-apatite in Cambrian strata in southern Israel.

91

92 Low-temperature thermochronology (LTT) is a powerful tool for quantitatively constraining  
93 the timing and rates of processes that disrupt the thermal regime of the upper crust over  
94 geological time scales (e.g. Reiners, 2005). Within the LTT toolbox, various  
95 thermochronometric systems have different temperature sensitivities. For zircon (U-Th)/He  
96 (ZHe), typically ~110-180°C (e.g. Wolfe & Stockli, 2010; Guenther et al., 2013), but lower  
97 in highly radiation damaged grains, for apatite fission track (AFT), typically ~60–110°C (e.g.  
98 Gleadow et al., 2002) and for apatite (U-Th)/He (AHe), ~–35 to >120°C [covering a range of  
99 radiation damaged grains and Cl content] (e.g. Shuster et al., 2006, Flowers et al., 2009;  
100 Gautheron et al., 2009; Djimbi et al., 2015). Tzifas et al. (2017) flagged the potential for  
101 fission-track dating of francolite, but to date no LTT data have been reported. This study  
102 investigates A-apatite genesis and thermal history using AFT, AHe and ZHe dating from  
103 Cambrian strata and underlying crystalline basement in the Nahal Shehoret and Eilat area,  
104 southern Israel, bordering the DST (Figure 1).

105

## 106 2 GEOLOGICAL SETTING AND SAMPLES

107

108 Following the Pan-African Orogeny, a thick sequence of shelf sediments accumulated over  
109 the northern margin of the Arabian-Nubian Shield through several depositional cycles. From  
110 Cambrian to Paleogene, recurrent eustatic oscillations caused minor hiatuses, whereas  
111 epeirogenic doming and subsequent truncation resulted in wide stratigraphic gaps. The most  
112 significant movement, in the Late Paleozoic, removed  $\geq 2.5$  km of Carboniferous to  
113 Ordovician strata from large areas in the Levant, and was accompanied by anomalously high  
114 geothermal gradients (e.g. Gvirtzman and Weissbrod, 1984; Kohn et al., 1992; Vermeesch et  
115 al., 2009). In southern Israel and southern Jordan, along the Dead Sea Rift margin marked by  
116 the DST, the sub-Cretaceous unconformity has superseded the Late Paleozoic (sub-Permian)  
117 unconformity, so that Lower Cretaceous siliciclastic rocks directly overlie Cambrian strata  
118 (Figures 1 and 2).

119

120 The DST separates the African (Sinai sub-plate) and the Arabian plates over a distance of  
121  $\sim 1000$  km, and relates the Red Sea spreading centre in the south to the Bitlis-Zagros zone of  
122 plate convergence in southern Turkey to the north. The matching of offsets of Precambrian to  
123 Paleogene stratigraphic markers, depositional patterns and tectonic elements on both sides of  
124 the DST indicate left-lateral displacement of  $\sim 105$  km (e.g. Quennell, 1958; Freund et al.,  
125 1970; Garfunkel, 1981). Different timetables have been proposed for the initiation and stages of  
126 DST movement (e.g. Quennell, 1958; Freund et al. 1970; Freund and Garfunkel, 1976; Bartov  
127 et al., 1980). However, Garfunkel (2014) summarised the evidence supporting early Miocene  
128 commencement of lateral motion along the DST (between 20 Ma and  $\sim 17$ – $16$  Ma). The slip  
129 history is strongly constrained by plate kinematics related to the opening of the Red Sea and the  
130 Gulf of Aden (e.g. Freund et al., 1970; Cochran, 1983; Joffe & Garfunkel, 1987). Further  
131 details of the geological history and stratigraphy of the study area are presented in several  
132 works (e.g. Weissbrod, 1980; Weissbrod, 2005; Vermeesch et al., 2009).

133

134 Studies of heavy minerals in the Paleozoic-Mesozoic clastic sequence ('Nubian Sandstone')  
135 on both sides of the DST were reported by Bender (1968), Weissbrod & Nachmias (1986)  
136 and Weissbrod & Bogoch (2007). Apatite is a common accessory in Cambrian siliciclastics,  
137 but is absent in the overlying series. D-apatite (fluorapatite) generally appears as subangular  
138 to rounded grains (typically up to  $200 \mu\text{m}$  in size) and more rarely, as prisms with rounded  
139 edges. D-apatites have euhedral overgrowths, some of which are A-apatite, which may  
140 contain opaque inclusions and may be coated with limonite. A-apatite (francolite) usually

141 occurs as basal hexagonal platelets (Figure 3). A-apatites are often associated with authigenic  
142 kaolinite, which may also be abundant in overlying Cretaceous strata, where no apatite is  
143 recorded.

144

### 145 3 SAMPLES AND METHODS

146

147 The Cambrian sequence in southern Israel is divided into four formations (Weissbrod, 2005).  
148 For this study, five samples of D-apatite from the Shehoret Formation and three from the  
149 overlying Netafim Formation (where A-apatite is common), were analysed for AFT, AHe  
150 and ZHe thermochronometry (Figure 1). Apatite, forming mm-size crystals in a pegmatite  
151 from underlying Neoproterozoic crystalline basement near Eilat (Figure 1) was also included  
152 for AFT and AHe analysis.

153

154 Mineral separations and analyses followed Gleadow et al. (2015), except that for ZHe  
155 analysis  $^{233}\text{U}$  and  $^{229}\text{Th}$  spikes were used. AFT measurements were made only on prismatic  
156 faces parallel to the c-axis (determined by orientation of track openings under reflected light).  
157 For A-AFT analysis, hexagonal plates were mounted ‘vertically’, so that measurements could  
158 also be made on prismatic faces, which ranged in width from ~80–125  $\mu\text{m}$ .

159

### 160 4 RESULTS

161 A- and D-AFT data, as well as AFT basement data, are presented in Table 1, with single grain  
162 radial plots and confined track-length histograms shown in Figure SI 1 (see also Tables SI 1  
163 and SI 2 for further AFT and chemical data). D-AFT and basement fission-track parameters  
164 span a limited range and clearly indicate total thermal resetting post-crystallisation/deposition.  
165 A-AFT data are markedly younger, yielding a central age of  $17.2 \pm 1.3$  Ma ( $1\sigma$ ), with longer  
166 mean track lengths (MTL) (Table 1). D-AHe ages on subrounded-rounded grains, ranging from  
167 ~11–207 Ma are younger than D-AFT ages, whereas A-AHe ages are Pliocene (weighted mean  
168  $3.2 \pm 0.4$  Ma at 95% CI) (Tables 2 and 3). The slight spread in AHe-A-apatite ages may indicate  
169 heterogeneity in U and Th content as reflected in the concentric growth pattern, affecting the  $\alpha$ -  
170 ejection correction. ZHe data predominantly yield Paleozoic ages from both D- and A-apatite  
171 bearing strata, with a negative age versus eU ppm correlation reflecting increased He diffusion  
172 in heavily radiation damaged grains (e.g. Guenther et al., 2013) (Figure 4 and Table 4).  
173 However, one grain in sample TW650 (in A-apatite-bearing strata), with exceptionally high eU

174 (>9000 ppm) yielded a ZHe age of  $17.3 \pm 1.1$  Ma, concordant with the coexisting A-AFT age.

175

## 176 5 DISCUSSION

177

178 Our D-AFT and D-AHe ages show similar trends to those of Vermeesch et al. (2009), although  
179 D-AFT MTL in that study were markedly lower. The wide dispersion of D-AHe ages probably  
180 reflects a range of factors (e.g. Table 4 in Wildman et al., 2016) and in this case may  
181 specifically include the influence of U-rich A-apatite overgrowths (either present or removed)  
182 on the age calculation. Time-temperature models for D-AFT using the HeFTy software  
183 (Ketchum, 2005) show a similar thermal history (Figure 5, see also Table SI 1 for model input  
184 data), including overprinting related to the late Devonian-early Carboniferous thermal event,  
185 constrained by the ZFT age in the Nahal Shehoret section reported by Vermeesch et al. (2009).

186

187 The A-AFT age data indicates that A-apatite growth was not directly linked to the late  
188 Devonian-early Carboniferous thermotectonic event. Rather, we suggest it resulted from  
189 intra-strata recrystallisation from low temperature, U-rich hydrothermal solutions, associated  
190 with early DST activity (e.g. Garfunkel, 2014). Further, a highly radiation-damaged zircon in  
191 sample TW650 yielded a ZHe age concordant with the co-existing A-AFT age. This suggests  
192 that highly-damaged zircons have the potential to record low-temperature thermal events  
193 driven by hydrothermal fluids (e.g. Mackintosh et al., 2017; Johnson et al., 2017).

194

195 Apatite is sensitive to a range of chemical and textural changes induced by fluids, over a  
196 broad range of pressures and temperatures (e.g. Harlov, 2015). The temperature of the fluids  
197 facilitating A-apatite growth was presumably relatively low with respect to the AFT  
198 temperature sensitivity range, because the D-AFT system in strata (and basement) proximal  
199 to predominantly A-apatite-bearing strata was not thermally overprinted to any extent in early  
200 Miocene time, although the widely dispersed D-AHe data do include some Miocene ages.

201

202 Cu-Mn-U mineralisation is associated with marine Cambrian phosphorite-bearing strata  
203 (Timna Formation) in the Timna Valley, southern Israel (Figure 1), where A-apatite-rich beds  
204 are also located (e.g. Bar-Matthews, 1987; Bar-Matthews & Matthews, 1990; Segev, 1992;  
205 Harlavan et al., 2017). Considerable debate has arisen over interpretation of field,  
206 petrographic and geochemical data related to mineralisation processes and their timing.

207 However, there is clear evidence for epigenetic dissolution (karstification) and mineralisation  
208 (including U-mobilisation and reprecipitation), also affecting crystalline basement, over a  
209 broad time span (e.g. Bar-Matthews, 1987; Segev et al., 1995, Beyth et al., 1997). Some  
210 mineralisation has been linked to the pattern of dense faulting and jointing, accompanied by  
211 the circulation of brines, associated with DST development (e.g. Beyth, 1987; Segev et al.,  
212 1995). Furthermore, altered Neoproterozoic gabbros in the Mt Timna Igneous Complex  
213 (Figure 1) acquired a chemical remanent magnetisation in the middle Miocene, which Marco  
214 et al. (1993) attributed to early DST-induced hydrothermal activity. The normal polarity  
215 suggests that alteration took place within a short time interval ( $< \sim 1$  m.y.), while the basement  
216 still resided under a sedimentary cover.

217  
218 Approximately two-thirds of total DST offset occurred by pure strike-slip movement until the  
219 end of the Miocene. Then, due to changes in regional plate kinematics, an additional minor  
220 transtensional or transpressional component resulted in some southern areas developing a more  
221 rift-like morphology (e.g. Garfunkel & Ben-Avraham, 2001; Smit et al., 2010), in part  
222 manifested as pull-apart basins, (e.g. Gulf of Eilat [Aqaba] and the Dead Sea). During this  
223 phase  $\sim 1$  km of Tertiary to Senonian section was removed from rift flanks bordering the DST  
224 and deposited in developing adjacent rift basins, as the prevailing drainage system was  
225 deepened (e.g. Avni et al., 2012). We therefore interpret Pliocene A-AHe ages as a cooling  
226 response related to removal of overburden along the southern rift margins, leading to  
227 exposure of the Cambrian section and underlying basement.

228  
229 In order to discern the temperature sensitivity of the A-AHe system, we carried out  
230 preliminary diffusion measurements on southern Israel A-apatite, supplemented by more  
231 detailed data from Yucca Mountain, USA A-apatite. The data indicate closure temperatures  
232 covering the two measurements of  $52^{\circ}\text{C}$  and  $56^{\circ}\text{C}$ , respectively (with a conservative  
233 uncertainty estimated at  $\sim 10^{\circ}\text{C}$ ), at a cooling rate of  $10^{\circ}\text{C}/\text{Myr}$  (Figure 6), which is lower  
234 than for typical igneous apatites (e.g. Farley, 2000). Considering this closure temperature  
235 range and a mean annual surface temperature of  $\sim 25^{\circ}\text{C}$ , a time-temperature model for LTT  
236 A-apatite data indicates that A-apatites have undergone  $\sim 35\text{-}40^{\circ}\text{C}$  of cooling in Pliocene time  
237 (Figure 5). Assuming a present-day geothermal gradient of  $\sim 20^{\circ}\text{C}/\text{km}$  in southern Israel  
238 (Eckstein & Simmons, 1977) would suggest that  $\sim 1.5\text{-}2$  km have been removed. However,  
239 any calculation of the thickness of cover removed based on these figures may be an  
240 overestimate, because deep faults associated with the rift system acted as conduits for hot

241 water ascending from deep aquifers, resulting in anomalously high heat flow (Eckstein &  
242 Simmons, 1977). The upper limit on the amount of Pliocene cooling must honor the co-  
243 existing early Miocene A-AFT age and MTL parameters; however, the temperature  
244 sensitivity of fission-track annealing for francolite is unknown and only nine track lengths  
245 were located for measurement. Assuming it is similar to fluorapatite, A-apatite would have  
246 resided under thermal conditions that preserved the A-AFT record from the early Miocene  
247 until Pliocene cooling.

248  
249 Our A-AFT and A-AHe dates are similar to ages recorded from ‘Mottled Zone’ outcrops to  
250 the north, in Israel and Jordan (Figure 1). This unique sequence of high temperature, low-  
251 pressure metamorphic rocks has a complex mineralogy (Gross, 1977) reflecting near-surface  
252 combustion metamorphism of late Cretaceous-early Tertiary bituminous chalk and marl (e.g.  
253 Kolodny & Gross, 1974; Burg et al., 1999). Combustion is linked to exposure and contact of  
254 these rocks with atmospheric oxygen, following uplift and erosion at the DST margins.  
255 Absolute dating indicates that combustion occurred in different areas at different times:  
256 gehlenite  $^{40}\text{Ar}/^{39}\text{Ar}$  at  $\sim 16.0 \pm 0.2$  Ma and anorthite-sanidine fels  $^{40}\text{Ar}/^{39}\text{Ar}$  at  $\sim 2.3\text{--}4.0$  Ma,  
257 (Gur et al., 1995), AFT age at  $13.6 \pm 2.0$  Ma (Kolodny et al., 1971). Gur et al. (1995) linked  
258 the early event to initial exposure of host rocks in the Miocene, and interpreted the Pliocene  
259 ages as a later combustion event related to removal of Neogene sediments and renewed  
260 exposure of bituminous rocks following initiation of the Dead Sea depression. ‘Mottled  
261 Zone’ geochronology therefore provides independent evidence for the timing of important  
262 DST-related events, and these events can be linked to those discerned in southern Israel (see  
263 Figure 7).

264

## 265 6 CONCLUSIONS

266

267 Detrital (D) and authigenic (A) apatites (francolite) are found in Cambrian strata in southern  
268 Israel. D-apatites preserve a similar low-temperature thermochronological history to  
269 underlying Neoproterozoic basement, reflecting Paleozoic-Mesozoic sedimentary cycles,  
270 marked by a distinct late Devonian-early Carboniferous thermal event. A-apatites, which may  
271 partially or totally replace D-apatite, record more recent geological events. A-AFT and ZHe  
272 (from a highly radiation-damaged zircon) data yield early Miocene ages ( $\sim 17$  Ma), while  
273 coexisting AHe ages are distinctly younger ( $\sim 3\text{--}4$  Ma). A-AFT and ZHe ages are interpreted

274 to reflect intra-strata recrystallisation driven by low-temperature hydrothermal solutions  
275 ascending through fractures created during early DST activity. We link our A-AHe ages to  
276 uplift and erosion of overlying cover during a transtensional DST phase, recording cooling  
277 due to removal of overburden during the Pliocene. The timing of two important milestones in  
278 DST movement is therefore recorded by A-apatite data in isolation. This timetable is also  
279 supported by independent chemical remanent magnetisation overprinting and mineralisation  
280 data in southern Israel and geochronology of the “Mottled Zone” to the north. This study  
281 invites further (U-Th)/He investigation of highly radiation-damaged zircons in southern Israel  
282 and other areas to evaluate the extent of early Miocene fluid-flow related to DST activity.

283

## 284 ACKNOWLEDGMENTS

285

286 The University of Melbourne thermochronology laboratory receives support under the  
287 AuScope program of the National Collaborative Research Infrastructure Strategy (NCRIS).  
288 Abaz Alimanovic (University of Melbourne) provided technical assistance with (U-Th)/He  
289 analyses. We are grateful to Kathryn Waltenberg for assistance in reviewing the A-apatite  
290 diffusion data. SB publishes with the permission of the Chief Executive Officer, Geoscience  
291 Australia. Maria Laura Balestrieri, Cécile Gautheron, and an anonymous reviewer are  
292 thanked for constructive comments and suggestions.

293

294

## 295 REFERENCES

296

297 Avni, Y., Segev, A., & Ginat, H. (2012). Oligocene regional denudation of the northern Afar  
298 dome: Pre- and syn-breakup stages of the Afro-Arabian Plate. *Geological Society of*  
299 *America Bulletin*, **124**, 1871–1897.

300 Bar-Matthews, M. (1987). The genesis of uranium in manganese and phosphorite  
301 assemblages, Timna Basin, Israel. *Geological Magazine*, **124**, 211–229.

302 Bar-Matthews, M., & Matthews, A. (1990). Chemical and stable isotope fractionation in  
303 manganese oxide-phosphorite mineralization, Timna Valley, Israel. *Geological*  
304 *Magazine*, **127**, 1–12.

- 305 Bartov, Y., Steinitz, G., Eyal, M., & Eyal, Y. (1980). Sinistral movement along the Gulf of  
306 Aqaba (Elat) – its age and relation to the opening of the Red Sea. *Nature*, **285**, 220–221.
- 307 Bender, F. (1968). *Geologie von Jordanien*. Gebrueder Borntraeger, Berlin, 230 pp.
- 308 Beyth, M. (1987). Mineralization related to rift systems: examples from the Gulf of Suez and  
309 the Dead Sea Rift. *Tectonophysics*, **141**, 191–197.
- 310 Beyth, M., Longstaffe, F. J., Ayalon, A., & Matthews, A. (1997). Epigenetic alteration of the  
311 Precambrian igneous complex at Mount Timna, southern Israel: Oxygen-isotope studies.  
312 *Israel Journal of Earth Sciences*, **46**, 1–11.
- 313 Bojar, A., Fritz, H., Kargl, S., & Unzog, W. (2002). Phanerozoic tectonothermal history of  
314 the Arabian-Nubian shield in the Eastern Desert of Egypt: Evidence from fission track  
315 and paleostress data. *Journal of African Earth Sciences*, **34**, 191–202.
- 316 Burg, A., Kolodny, Y., & Lyakhovsky, V. (1999). Hatrurim-2000: “The Mottled Zone”  
317 revisited 40 years later. *Israel Journal of Earth Sciences*, **48**, 209–223.
- 318 Cochran, J. R. (1983). A model for the development of the Red Sea. *American Association of*  
319 *Petroleum Geologists Bulletin*, **67**, 41–49.
- 320 Djimbi, D. M., Gautheron, C., Roques, J., Tassan-Got, L., Gerin, C., & Simoni, E. (2015).  
321 Impact of apatite chemical composition on (U-Th)/He thermochronometry: An atomistic  
322 point of view. *Geochimica et Cosmochimica Acta*, **167**, 162–176.
- 323 Eckstein, Y., & Simmons, G. (1977). Measurement and interpretation of terrestrial heat flow  
324 in Israel. *Geothermics*, **6**, 117–141.
- 325 Farley, K. A. (2000). Helium diffusion from apatite: general behavior as illustrated by  
326 Durango fluorapatite. *Journal of Geophysical Research*, **105**, 2903–2914.
- 327 Farley, K. A., Wolf, R. A., & Silver, L. T. (1996). The effects of long alpha-stopping on (U–  
328 Th)/He ages. *Geochimica et Cosmochimica Acta*, **21**, 4223–4229.
- 329 Fechtig, H., & Kalbitzer, S. (1996). The diffusion of argon in potassium-bearing solids. In:  
330 Schaeffer, O. A. & Zähringer, J. (Eds.), *Potassium-Argon Dating*. Springer-Verlag, New  
331 York, pp. 68–107.
- 332 Flowers, R. M., Ketcham, R. A., Shuster, D. L., & Farley, K. A. (2009). Apatite (U–Th)/He  
333 thermochronometry using a radiation damage accumulation and annealing model.  
334 *Geochimica et Cosmochimica Acta*. **73**, 2347–2365.

- 335 Freund, R., & Garfunkel, Z. (1976). *Guidebook to the Dead Sea Rift*. Department of Geology,  
336 Hebrew University, Jerusalem, 27 pp.
- 337 Freund, R., Garfunkel, Z., Zak, I., Goldberg, M., Weissbrod, T., Derin, B., Bender, F.,  
338 Wellings, F. E., & Girdler, R. W. (1970). The shear along the Dead Sea rift [and  
339 Discussion]. *Philosophical Transactions of the Royal Society London, Series A,*  
340 *Mathematical and Physical Sciences*, **267**, 107–130.
- 341 Galbraith, R. F. (1990). The radial plot: graphical assessment of spread in ages. *Nuclear*  
342 *Tracks and Radiation Measurements*, **17**, 207–214.
- 343 Galbraith, R. F. (2005). *Statistics for Fission Track Analysis*. Taylor & Francis Group, Boca  
344 Raton, 219 pp.
- 345 Garfunkel, Z. (1981). Internal structure of the Dead Sea leaky transform (rift) in relation to  
346 plate kinematics. *Tectonophysics*, **80**, 81–108.
- 347 Garfunkel, Z. (2014). Lateral motion and deformation along the Dead Sea Transform. In:  
348 Garfunkel, Z., Ben-Avraham, Z., & Kagan, E. (Eds.), *Dead Sea Transform Fault System:*  
349 *Reviews. Modern Approaches in Solid Earth Sciences*, **6**. Springer Science and Business  
350 Media, Dordrecht, pp. 109–150.
- 351 Garfunkel, Z. & Ben-Avraham, Z. (2001). Basins along the Dead Sea Transform. In: Ziegler,  
352 P. A., Cavazza, W., Robertson, A. H. F., & Crasquin-Soleau, S. (Eds.), *Peri-Tethys*  
353 *Memoir 6: Peri-Tethyan Rift/Wrench Basins and Passive Margins*. Mémoires du  
354 Muséum National d’Histoire Naturelle **186**. Publications Scientifiques du Muséum,  
355 Paris, pp. 607–627.
- 356 Gautheron, C., Tassan-Got, L., Barbarand, J., & Pagel, M. (2009). Effect of alpha-damage  
357 annealing on apatite (U–Th)/He thermochronology. *Chemical Geology*, **266**, 157–170.
- 358 Gleadow, A. J. W., Belton, D. X., Kohn, B. P., & Brown, R. W. (2002). Fission track dating  
359 of phosphate minerals and the thermochronology of apatite. In: Kohn, M. P., Rakovan,  
360 J., & Hughes, J. M. (Eds.), *Phosphates: Geochemical, Geobiological, and Materials*  
361 *Importance*. Reviews in Mineralogy and Geochemistry, **48**, Mineralogical Society of  
362 America, pp. 579–630.
- 363 Gleadow, A. J. W., Gleadow, S. J., Belton, D. X., Kohn, B. P., Krochmal, M. S., & Brown,  
364 R. W. (2009). Coincidence mapping – a key strategy for the automatic counting of  
365 fission tracks in natural minerals. In: Lisker, F., Ventura, B., & Glasmacher, U. A.

- 366 (Eds.), *Thermochronological Methods: From Palaeotemperature Constraints to*  
367 *Landscape Evolution Models*. Geological Society, London Special Publication, **324**, pp.  
368 25–36.
- 369 Gleadow, A., Harrison, M., Kohn, B., Lugo-Zazueta, R., & Phillips, D. (2015). The Fish  
370 Canyon Tuff: A new look at an old low-temperature thermochronology standard. *Earth*  
371 *and Planetary Science Letters*, **424**, 95–108.
- 372 Golan, T., Katzir, Y., & Coble, M. A. (2018). Early Carboniferous anorogenic magmatism in  
373 the Levant: implications for rifting in northern Gondwana. *International Geology*  
374 *Review*, **60**, 101–108.
- 375 Guenther, W. R., Reiners, P. W., Ketchum, R. A., Nasdala, L., & Giester, G. (2013). Helium  
376 diffusion in natural zircon: Radiation damage, anisotropy, and the interpretation of zircon  
377 (U-Th)/He thermochronology. *American Journal of Science*, **313**, 145–198.
- 378 Gur, D., Steinitz, G., Kolodny, Y., Starinsky, A., & McWilliams, M. (1995).  $^{40}\text{Ar}/^{39}\text{Ar}$  dating  
379 of combustion metamorphism (“Mottled Zone”, Israel). *Chemical Geology (Isotope*  
380 *Geoscience Section)*, **122**, 171–184.
- 381 Gross, S. (1977). The mineralogy of the Hatrurim Formation, Israel. *Israel Geological Survey*  
382 *Bulletin*, **70**, 80 pp.
- 383 Gvirtzman, G., & Weissbrod, T. (1984). The Hercynian Geanticline of Helez and the Late  
384 Palaeozoic history of the Levant. In: Dixon, J. E., & Robertson, A. H. F. (Eds.), *The*  
385 *Geological Evolution of the Eastern Mediterranean*. Geological Society, London Special  
386 Publication, **17**, pp. 177–186.
- 387 Harlavan, Y., Bar-Matthews, M., Matthews, A., Asael, D., & Segal, I. (2017). Tracing the  
388 sources of sedimentary Cu and Mn ores in the Cambrian Timna Formation, Israel using  
389 Pb and Sr isotopes. *Journal of Geochemical Exploration*, **178**, 67–82.
- 390 Harlov, D. E. (2015). Apatite: A fingerprint for metasomatic processes. *Elements*, **11**, 171–  
391 175.
- 392 Hasebe, N., Barbarand, J., Jarvis, K., Carter, A., & Hurford, A. J. (2004). Apatite fission-  
393 track chronometry using laser ablation ICP-MS. *Chemical Geology*, **207**, 134–145.
- 394 Heimann, A., Eyal, Y., Eyal, M., & Foland, K. F. (1995). Thermal events and low  
395 temperature alteration in the Precambrian schistose dykes and their host rocks in the Eilat

- 396 area, southern Israel:  $^{40}\text{Ar}/^{39}\text{Ar}$  geochronology. In: Baer, G., & Heimann, A. (Eds.),  
397 *Physics and Chemistry of Dykes*. Rotterdam, Balkema, pp. 281–292.
- 398 Joffe, S., & Garfunkel, Z. (1987). Plate kinematics of the circum Red Sea—a re-evaluation.  
399 *Tectonophysics*, **141**, 5–22.
- 400 Johnson, J. E., Flowers, R. M., Baird, G. B., & Mahan, K. H. (2017). “Inverted” zircon and  
401 apatite (U–Th)/He dates from the Front Range, Colorado: High-damage zircon as a low-  
402 temperature (<50 °C) thermochronometer. *Earth and Planetary Science Letters*, **466**, 80–  
403 90.
- 404 Ketcham, R. A. (2005). Forward and inverse modeling of low-temperature  
405 thermochronometry data. In: Reiners, P. W., & Ehlers, T. A. (Eds.), *Low-Temperature*  
406 *Thermochronology: Techniques, Interpretations, and Applications*. Reviews in  
407 *Mineralogy and Geochemistry*, **58**, Mineralogical Society of America, pp. 275–314.
- 408 Ketcham, R. A., Carter, A., Donelick, R. A., Barbarand, J., & Hurford, A. J. (2007).  
409 Improved modeling of fission-track annealing in apatite. *American Mineralogist*, **92**, 799–  
410 810.
- 411 Kolodny, Y., & Gross, S. (1974). Thermal metamorphism by combustion of organic matter:  
412 isotopic and petrological evidence. *Journal of Geology*, **82**, 489–506.
- 413 Kolodny, Y., Bar, M., & Sass, E. (1971). Fission track age of the ‘Mottled Zone Event’ in  
414 Israel. *Earth and Planetary Science Letters*, **11**, 269–272.
- 415 Kohn, B. P., Eyal, M., & Feinstein, S. (1992). A major Late Devonian–Early Carboniferous  
416 (Hercynian) thermotectonic event at the NW margin of the Arabian-Nubian shield:  
417 Evidence from zircon fission track dating. *Tectonics*, **11**, 1018–1027.
- 418 Mackintosh, V., Kohn, B., Gleadow, A., & Tian, Y. (2017). Phanerozoic morphotectonic  
419 evolution of the Zimbabwe Craton: unexpected outcomes from a multiple low-  
420 temperature thermochronology study. *Tectonics*, **36**, 1–24.
- 421 Marco, S., Ron, H., Matthews, A., Beyth, M., & Navon, O. (1993). Chemical remanent  
422 magnetism related to the Dead Sea Rift: Evidence from Precambrian igneous rocks on  
423 Mount Timna, southern Israel. *Journal of Geophysical Research*, **98**, 16001–16012.
- 424 McClellan, G. H., & Van Kauwenbergh, S. J. (1990). Mineralogy of sedimentary apatites. In:  
425 Notholt, A. J. G., & Jarvis, I. (Eds.), *Phosphorite Research and Development*. Geological  
426 Society, London Special Publication, **52**, pp. 23–31.

- 427 McDowell, F. W., McIntosh, W. C., & Farley, K. A. (2005). A precise  $^{40}\text{Ar}$ - $^{39}\text{Ar}$  reference  
428 age for the Durango apatite (U-Th)/He and fission track dating standard. *Chemical*  
429 *Geology*, **214**, 249–263.
- 430 Paton, C., Hellstrom, J., Paul, B., Woodhead, J., & Hergt, J. (2011). Iolite: Freeware for the  
431 visualisation and processing of mass spectrometric data. *Journal of Analytical Atomic*  
432 *Spectrometry*, **26**, 2508–2518.
- 433 Quennell, A. M. (1958). The structural and geomorphic evolution of the Dead Sea rift.  
434 *Quarterly Journal of the Geological Society of London*, **114**, 2–24.
- 435 Reiners, P. W. (2005). Zircon (U-Th)/He thermochronometry. In: Reiners, P. W., & Ehlers,  
436 T. A. (Eds.), *Low-Temperature Thermochronology: Techniques, Interpretations, and*  
437 *Applications*. Reviews in Mineralogy and Geochemistry, **58**, Mineralogical Society of  
438 America, pp. 151–179.
- 439 Shuster, D. L., Flowers, R. M., & Farley, K. A. (2006). The influence of natural radiation  
440 damage on helium diffusion kinetics in apatite. *Earth and Planetary Science Letters*, **249**,  
441 148–161.
- 442 Segev, A. (1992). Remobilization of uranium and associated metals through karstification  
443 processes: A case study from the Timna formation (Cambrian), Southern Israel. *Ore*  
444 *Geology Reviews*, **7**, 135–148.
- 445 Segev, A., Halicz, L., Steinitz, G., & Lang, B. (1995). Postdepositional processes on a buried  
446 Cambrian sequence in southern Israel, north Arabian Massif: Evidence from new K-Ar  
447 dating of Mn-nodules. *Geological Magazine*, **132**, 375–385.
- 448 Smit, J., Brun, J. P., Cloetingh, S., & Ben-Avraham, Z. (2010). The rift-like structure and  
449 asymmetry of the Dead Sea Fault. *Earth and Planetary Science Letters*, **290**, 74–82.
- 450 Tzifas, I. T., Glasmacher, U. A., Misaelides, P., Godelitsas, A., Gamaletsos, P. N.,  
451 Goettlicher, J., & Franoso de Godoy, D. (2017). Uranium-bearing francolites present in  
452 organic-rich limestones of NW Greece: a preliminary study using synchrotron radiation  
453 and fission track techniques. *Journal of Radioanalytical and Nuclear Chemistry*, **311**,  
454 465–472.
- 455 Vermeesch, P. (2009). RadialPlotter: a Java application for fission track, luminescence and  
456 other radial plots. *Radiation Measurements*, **44**, 409–410.

- 457 Vermeesch, P., Avigad, D., & McWilliams, M. O. (2009). 500 m.y. of thermal history  
458 elucidated by multi-method detrital thermochronology on north Gondwana sandstone  
459 (Eilat area, Israel). *Geological Society of America Bulletin*, **121**, 1204–1216.
- 460 Weissbrod, T. (1980). The Paleozoic of Israel and adjacent countries. Unpublished PhD  
461 dissertation, Hebrew University, Jerusalem, 275 pp. (in Hebrew).
- 462 Weissbrod, T. (2005). The Paleozoic in Israel and environs. In: Hall, J. K., Krashennikov,  
463 V. A., Hirsch, F., Benjamini, C., and Flexer, A. (Eds.), *Geological Framework of the*  
464 *Levant Volume II: The Levantine Basin and Israel*. Historical Productions-Hall,  
465 Jerusalem, pp. 283–316.
- 466 Weissbrod, T., & Bogoch, R. (2007). Distribution pattern and provenance implications of the  
467 heavy minerals in Neoproterozoic to Mesozoic siliciclastic successions in the Arabo-  
468 Nubian Shield and its northern periphery: A review. In: Mange, M. A., & Wright, D. T.  
469 (Eds.), *Heavy Minerals in Use*. Developments in Sedimentology, **58**, pp. 647–676.  
470 Elsevier, Amsterdam.
- 471 Weissbrod, T., & Nachmias, J. (1986). Stratigraphic significance of heavy minerals in the late  
472 Precambrian-Mesozoic clastic sequence (“Nubian Sandstone”) in the Near East.  
473 *Sedimentary Geology*, **47**, 263–291.
- 474 Weissbrod, T., Perath, I., & Nachmias, J. (1987). Apatite as a paleoenvironmental indicator  
475 in the Precambrian-Mesozoic clastic sequence of the Middle East. *Journal of African*  
476 *Earth Sciences*, **6**, 797-805.
- 477 Wildman, M., Brown, R., Beucher, R., Persano, C., Stuart, F., Gallagher, K., Schwanethal, J.,  
478 & Carter, A. (2016). The chronology and tectonic style of landscape evolution along the  
479 elevated Atlantic continental margin of South Africa resolved by joint apatite fission  
480 track and (U-Th-Sm)/He thermochronology. *Tectonics*, **35**, 511–545.
- 481 Wolfe, M. R., & Stockli, D. F. (2010). Zircon (U-Th)/He thermochronometry in the KTB  
482 drill hole, Germany, and its implications for bulk He diffusion kinetics in zircon. *Earth*  
483 *and Planetary Science Letters*, **295**, 69–82.
- 484
- 485
- 486
- 487

488  
489  
490  
491  
492  
493  
494  
495  
496  
497  
498  
499  
500  
501  
502  
503  
504  
505  
506  
507  
508  
509  
510  
511  
512  
513  
514  
515  
516

# Author Manuscript

517

518

519

520

## 521 FIGURE CAPTIONS

522

523

524 **Figure 1.** Locality map. Mt TIC = Mt Timna Igneous Complex. A stratigraphic section at  
525 Nahal Shehoret, showing positions of samples analysed and types of low temperature  
526 thermochronology methods carried out on them. Numbers following formation names can be  
527 keyed into those indicated in the section photo in Figure 2. Stars next to sample numbers  
528 indicate those that contain A-apatite.

529

530 **Figure 2.** Cambrian sedimentary type locality in Nahal Shehoret valley (see also Figure 1).  
531 Foreground shows the Multicolored Member (1) of the Shehoret Formation, consisting of  
532 alternating beds of coarse- to fine-grained, cross-bedded subarkose and laminated clays  
533 displaying a range of colors. Background shows the cliff-forming White (2) and Variegated  
534 (3) (red-brown) members of the Shehoret Formation, comprising uniformly fine-grained and  
535 thinly cross-bedded subarkose. These strata are overlain by red-brown fine- to medium-  
536 grained and cross-bedded quartz-arenite of the Netafim Formation (4), which in turn is  
537 overlain unconformably by the Lower Cretaceous Amir Formation (5) at top. Note recent  
538 gravel beds on the valley floor between units (1) and (2).

539

540 **Figure 3.** a) Scanning electron microscope image showing hexagonal A-apatite with small  
541 particles of kaolinite in sample TW650. Grains typically range from ~50-400  $\mu\text{m}$  in diameter,  
542 though well-developed prisms and twin crystals also occur. A-apatites are typically U-rich,  
543 display undulatory extinction when observed down the c-axis, sometimes show concentric  
544 lamellae and effervesce upon dissolution in weak  $\text{HNO}_3$ . These are all characteristics of  
545 carbonate-rich fluorapatite (francolite). b) Spontaneous fission tracks in A-apatite sample  
546 TW650. c) Spontaneous fission tracks in D-apatite sample TW558.

547

548 **Figure 4.** a) Plot of single grain AHe age versus effective uranium content (eU) ppm from  
549 Cambrian sedimentary samples, which are predominantly either D- or A-apatite-bearing (see

550 Tables 2-3). The general negative relationship, with younger ages generally related to  
551 increased eU content, reflects the effect of radiation damage on He diffusion (e.g. Shuster et  
552 al., 2006; Flowers et al., 2009 and Gautheron et al., 2009). b) Plot of single grain ZHe age  
553 versus effective uranium content (eU) ppm from Cambrian sedimentary samples, which are  
554 predominantly either D- or A-apatite-bearing (see Table 4). Oldest zircon ages at low eU  
555 (ppm) may reflect primary Neoproterozoic Pan African Orogeny cooling ages, but a negative  
556 relationship between single grain age and increased eU content (which is a proxy for  
557 radiation-damage), shown more clearly in the upper panel, is the product of increased He  
558 diffusivity. Note that for one grain with very high eU, the ZHe age of  $17.3 \pm 1.1$  Ma is  
559 concordant with an A-AFT age from the same sample (see text for further discussion).

560

561 **Figure 5.** Thermal history reconstructions of representative samples analysed using HeFTy  
562 software (Ketcham, 2005 and fission-track annealing model of Ketcham et al., 2007 and  
563 where applicable for sample TW650 using the He diffusion model of Flowers et al., 2009).  
564 Measured and model ages are compared, together with GOF = Goodness of Fit for best-fit  
565 time-temperature paths, which are represented by a dark solid line within the statistical good-  
566 fit envelope (magenta), which represents good models that fall within a probability >50% (a  
567 weighted mean path for this envelope is also shown). Also displayed is an outer envelope  
568 (green), which represents accepted models that fall within a probability of 5%. The right-  
569 hand panels show measured and model MTL ( $n$  = number of length measurements) and c-  
570 axis projected confined track lengths illustrated as histograms and the smoothed probability  
571 distributions representing the model track lengths from the “best-fit” models. Broad time-  
572 temperature constraints used were as follows. Cambrian stratigraphic age or nominal Pan-  
573 African age for basement, partial annealing of zircon fission tracks for Nahal Shehoret section  
574 during late Devonian-early Carboniferous time (see text). Following that constraints are related  
575 to the amount of erosion estimated in accordance with the thickness of the various formations  
576 in Israel and adjacent regions. Since Pan-African orogeny the sedimentary column of  
577 southern Israel has been affected by four main epeirogenic events, which are expressed by  
578 notable unconformities with conspicuous rate of truncation (beside numerous  
579 disconformities). The rate of truncation of each event was calculated according to the  
580 thickness of the missing sequence (formations) from the bounding flanks of the DST while  
581 they are still preserved in close or remote areas in southern Israel (Permian to Miocene) and  
582 adjacent countries such as southern Jordan, northwestern Saudi Arabia and Sinai (also  
583 Ordovician to Carboniferous), which in keeping with their sedimentary shelf characteristics

584 and the paleogeography should have been deposited over the whole Near East, but have been  
585 removed from large areas in the Levant including the DST rift shoulders. Present day mean  
586 surface temperature is assumed to be  $\sim 20\text{--}25^\circ\text{C}$ . Note no ZFT data are available from  
587 basement sample (EP2), located  $\sim 10$  km south of Nahal Shehoret and in this case modelling  
588 indicates only partial Paleozoic overprinting of the AFT system to  $\sim 80\pm 5^\circ\text{C}$  (Figure 6). Note  
589 for sample TW650 only nine track lengths were available for measurement.

590  
591 **Figure 6.** Results of He step-heating diffusion experiments carried out on hexagonal  
592 francolite in the Cambrian Netafim Formation, southern Israel (at the University of  
593 Melbourne) and from Tertiary ash-flow tuffs, Yucca Mountain, Nevada (at Caltech). Initial  
594 diffusivities are lower than the extrapolation of values at higher temperatures. This is  
595 commonly observed in apatites and is attributed to rounding of the initial concentration  
596 profile by  $\alpha$ -ejection and possibly by diffusion (e.g. Fechtig & Kalbitzer, 1996; Farley,  
597 2000). Between  $\sim 200\text{--}300^\circ\text{C}$  the diffusivity lies on a linear array (independent of any  
598 temperature cycling), which is consistent with thermally activated volume diffusion implying  
599 a closure temperature for the two measurements of  $52^\circ\text{C}$  and  $56^\circ\text{C}$  (with a conservative  
600 uncertainty of  $\sim 10^\circ\text{C}$ ) at a cooling rate of  $10^\circ\text{C}/\text{Myr}$ . Step heating data and calculations of  
601 parameters arising from the diffusion experiments are presented in Table SI 3.

602  
603 **Figure 7.** Schematic summary timetable relating the proposed time-temperature history of A-  
604 apatite (and one ZHe measurement) in southern Israel, deduced from low-temperature  
605 thermochronology data, to major phases of DST motion and other independent geological  
606 information (see text). Phase I relates to initial early-late Miocene strike-slip DST  
607 movement, resulting in about two-thirds of the total  $\sim 105$  km displacement. Phase II relates  
608 to the onset of a more transtensional environment along the DST resulting in more of a rift  
609 morphology, with erosion of the rift flanks filling adjacent pull-apart basins, leading to  
610 cooling and exposure of Cambrian sediments and underlying crystalline basement. D-AHe  
611 ages are widely dispersed. CRM = chemical remanent magnetisation and M-Zone = timing of  
612 combustion events dated from the “Mottled Zone” (see text for further discussion).

**Table 1.** Apatite fission track data.

Sample No.	Lithology/Formation	Location (Long E/Lat N)	No. of grains	N <sub>s</sub>	ρ <sub>s</sub> [10 <sup>5</sup> cm <sup>-2</sup> ]	<sup>238</sup> U [ppm ± 1σ]*	Pooled age [Ma ± 1σ]	Central age [Ma ± 1σ]	N <sub>length</sub>	Mean track length [μm ± se]	St.Dev. [μm]	D <sub>par</sub> [μm]*
<b>Authigenic (Cambrian)</b>												
TW650	Netafim Fm	34°57' / 29°38'	46	463	4.36E+05	50.99 ± 18.57	17.0 ± 1.7 Ma	17.2 ± 1.3 Ma	9	13.82 ± 0.48	1.45	1.80 ± 0.46
<b>Detrital (Cambrian)</b>												
TW558	Shehoret Fm (White Mbr)	34°56' / 29°38'	24	2819	3.605E+06	23.39 ± 13.57	299.8 ± 15.5	313.4 ± 14.2	147	11.68 ± 0.12	1.47	1.59 ± 0.24
TW560	Shehoret Fm (White Mbr)	34°56' / 29°38'	36	3044	3.242E+06	22.50 ± 12.98	282.0 ± 11.3	289.0 ± 11.8	112	11.34 ± 0.13	1.41	1.54 ± 0.17
TW670	Shehoret Fm (White Mbr)	34°56' / 29°38'	30	1484	2.997E+06	21.57 ± 15.17	274.3 ± 12.3	279.1 ± 12.2	60	11.31 ± 0.19	1.48	1.95 ± 0.57
TW683	Shehoret Fm (White Mbr)	34°56' / 29°38'	27	1524	3.782E+06	28.97 ± 20.20	259.1 ± 16.8	266.9 ± 15.5	45	11.16 ± 0.25	1.71	1.56 ± 0.15
TW836	Shehoret Fm (Multicolored Mbr)	34°56' / 29°38'	10	321	1.802E+06	10.64 ± 7.04	328.1 ± 36.1	337.4 ± 32.4	51	11.29 ± 0.20	1.43	1.47 ± 0.16
<b>Basement (Neoproterozoic)</b>												
EP-2	Elat pegmatite	34°56' / 29°34'	13	2718	1.127E+07	59.38 ± 23.58	364.4 ± 12.4	366.3 ± 11.0	119	11.78 ± 0.13	1.46	1.63 ± 0.10

N<sub>s</sub> = number of spontaneous tracks counted; ρ<sub>s</sub> = spontaneous track density; N<sub>length</sub> = number of confined lengths measured; se = standard error; D<sub>par</sub> = long axis of track etch pit;

\*Uncertainty is standard deviation of mean

**Notes:** Apatite grains were mounted and polished, and fission tracks analysed using the LA-ICP-MS technique following procedures described in Gleadow et al. [2015].

Analyses were performed on image sets captured by the software *TrackWorks*. Spontaneous track densities were measured on prismatic internal apatite surfaces after etching with 5M HNO<sub>3</sub> for 20 sec at 20°C.

Track counts were obtained by automated counting using the software *FastTracks* employing the 'coincidence mapping' technique of Gleadow et al. (2009) followed by manual inspection.

Uranium concentrations of each grain were determined by LA-ICP-MS single spot analysis using a New Wave Nd:YAG Laser (λ= 213nm with 5Hz @ 50% power, spot size = 30μm) connected to an Agilent 7700 mass spectrometer.

NIST612 was used as the primary LA-ICP-MS standard, together with a sintered Mud Tank Carbonatite apatite as an in-house secondary reference material.

Data reduction of LA-ICP-MS results was performed using the TraceElement\_IS data reduction scheme in software package *Iolite* [Paton et al., 2011]. Single grain and pooled ages were calculated according to Hasebe et al. (2004).

Central ages were estimated from single grain ages and errors according to the formulas given by Galbraith (2005, p.100) using the Newton-Raphson method. All ages are 'model' ages obtained using a range factor (R<sub>s</sub>) of 7.50 μm.

Confined track lengths (TINTS) were measured as true 3D lengths using *FastTracks* and are corrected for a refractive index of 1.634 for apatite.

**Table 2.** Single grain apatite (U-Th-Sm)/He data for detrital and crystalline basement apatite.

Sample No.	Lab. No.	He#	<sup>4</sup> He (ncc)	Mass (mg)	<sup>a</sup> Mean F <sub>r</sub>	U ppm	Th ppm	Sm ppm	Th/U	<sup>b</sup> [eU] ppm	Corrected age (Ma)	Error (±1σ)	Grain length (μm)	Grain half width (μm)	<sup>c</sup> Rs	<sup>d</sup> Grain morphology
<b>Detrital (Cambrian)</b>																
TW558	14392	46447	0.573	0.0068	0.76	23.2	40.6	54.1	1.75	32.7	27.6	1.7	213.1	56.3	66.8	OT
TW558	14393	46450	2.037	0.0106	0.81	7.9	5.2	94.2	0.66	9.1	206.9	12.8	220.0	69.3	79.1	OT
TW558	14394	46453	0.724	0.0064	0.78	11.9	8.3	314.6	0.69	13.9	83.1	5.2	168.9	61.6	67.7	OT
TW558	14395	46456	0.435	0.0042	0.73	8.0	11.3	34.2	1.42	10.7	108.1	6.7	176.6	48.9	57.4	OT
TW558	14396	46459	0.056	0.0078	0.78	3.1	4.1	95.2	1.33	4.1	18.0	1.1	192.5	63.6	71.7	OT
TW560	14413	46462	1.350	0.0105	0.82	106.7	15.3	63.9	0.14	110.3	11.7	0.7	136.3	87.6	80.0	OT
TW560	14415	46468	0.650	0.0077	0.79	49.6	5.7	94.7	0.11	50.9	17.2	1.1	99.7	87.5	69.9	OT
TW560	14416	46471	0.147	0.0037	0.72	23.8	17.5	226.4	0.73	27.9	15.8	1.0	171.2	46.6	54.9	OT
TW560	14417	46474	0.080	0.0113	0.81	5.5	5.1	36.6	0.94	6.7	10.6	0.7	199.7	75.0	81.8	OT
TW560	14418	46477	0.911	0.0072	0.78	8.8	7.8	20.4	0.89	10.6	125.1	7.8	192.2	60.8	69.3	OT
TW670	18757	62411	0.068	0.00264	0.70	15.2	16.0	227.3	1.05	19.0	15.8	1.0	114.0	48.0	50.6	OT
TW670	18758	62414	0.680	0.00193	0.65	37.5	59.2	441.1	1.58	51.4	85.1	5.3	114.2	41.0	45.2	OT
TW670	18759	62417	0.133	0.00133	0.59	9.4	41.4	220.6	4.39	19.1	71.4	4.4	109.1	34.8	39.6	OT
TW670	18760	62420	0.121	0.00171	0.63	14.1	43.8	169.3	3.10	24.4	37.2	2.3	104.0	40.5	43.7	OT
TW670	18761	62423	0.974	0.00226	0.69	52.2	20.0	294.8	0.38	56.9	88.9	5.5	83.2	52.0	48.0	OT
TW670	18762	62426	0.091	0.00280	0.70	21.1	15.1	201.7	0.72	24.6	15.3	0.9	80.9	58.6	51.0	OT
TW670	18763	62429	0.700	0.01311	0.82	5.5	5.9	57.9	1.06	6.9	76.1	4.7	185.1	83.9	86.6	OT
TW670	18764	62432	2.475	0.00482	0.76	33.1	17.6	282.5	0.53	37.2	146.9	9.1	150.3	56.5	61.6	OT
<b>Basement (Neoproterozoic)</b>																
EP-2	18750	62393	92.569	-	1.00	-	-	-	0.78	-	390.1	24.2	-	-	-	-
EP-2	18751	62396	54.245	-	1.00	-	-	-	0.74	-	458.2	28.4	-	-	-	-
EP-2	18752	62399	35.246	-	1.00	-	-	-	0.38	-	327.3	20.3	-	-	-	-
EP-2	18753	62402	37.197	-	1.00	-	-	-	0.76	-	289.4	17.9	-	-	-	-
EP-2	18754	62405	22.686	-	1.00	-	-	-	0.27	-	205.3	12.7	-	-	-	-
EP-2	18755	62408	113.722	-	1.00	-	-	-	0.41	-	442.5	27.4	-	-	-	-
<b>Durango apatite</b>																
Durango	14466	46390	6.379	-	1.00	-	-	-	22.86	-	31.7	2.0	-	-	-	-
Durango	14467	46519	2.452	-	1.00	-	-	-	20.81	-	31.0	1.9	-	-	-	-
Durango	14527	46554	6.289	-	1.00	-	-	-	21.16	-	31.3	1.9	-	-	-	-
Durango	18756	62380	4.628	-	1.00	-	-	-	16.31	-	31.5	2.0	-	-	-	-
Durango	18793	62489	3.895	-	1.00	-	-	-	21.34	-	31.8	2.0	-	-	-	-

**Table 2.** Single grain apatite (U-Th-Sm)/He data for detrital and crystalline basement apatite.

<sup>a</sup>F<sub>ij</sub> is the  $\alpha$ -ejection correction after Farley et al. (1996).

<sup>b</sup>Effective uranium content [U ppm + 0.235\*Th ppm].

<sup>c</sup>Radius of the equivalent sphere of the crystal.

<sup>d</sup>Grain morphology - 0T = no crystal terminations, 1T = one crystal termination and 2T = 2 crystal terminations.

**Note:** Durango apatite reference material (31.02±1.01 Ma - McDowell et al., 2005) was run as an internal check with each batch of apatites analysed.

Author Manuscript

**Table 3.** Single grain authigenic apatite (U-Th-Sm)/He data.

Sample	Lab. No.	He#	<sup>4</sup> He (ncc)	Mass (mg)	<sup>a</sup> Mean F <sub>T</sub>	U ppm	Th ppm	Sm ppm	Th/U	<sup>b</sup> [eU] ppm	Corrected age (Ma)	Error (±1σ)	Grain plate thickness parallel c-axis (μm)	Grain plate width perpendicular c-axis (μm)
TW650	14420	46483	0.164	0.0216	0.82	17.0	25.3	41.4	1.49	22.9	<b>3.3</b>	<b>0.2</b>	92.8	304.7
TW650	14421	46486	0.355	0.0282	0.83	20.9	82.0	36.9	3.92	40.2	<b>3.1</b>	<b>0.2</b>	107.0	324.0
TW650	14422	46489	0.206	0.0220	0.82	23.5	32.5	53.6	1.38	31.1	<b>3.0</b>	<b>0.2</b>	89.5	312.6
TW650	14423	46492	0.157	0.0142	0.79	26.2	25.1	49.8	0.96	32.1	<b>3.6</b>	<b>0.2</b>	73.8	277.1
TW650	14424	46495	0.156	0.0240	0.82	16.9	20.7	40.3	1.22	21.8	<b>3.0</b>	<b>0.2</b>	92.7	321.2
TW650	14425	46498	0.166	0.0285	0.83	19.4	18.1	38.9	0.94	23.7	<b>2.5</b>	<b>0.2</b>	94.8	345.8
TW651	14432	46501	0.108	0.0068	0.74	28.7	46.4	155.2	1.62	39.6	<b>4.4</b>	<b>0.3</b>	66.0	203.1
TW651	14433	46504	0.134	0.0082	0.75	32.8	147.6	150.1	4.50	67.5	<b>2.7</b>	<b>0.2</b>	70.0	215.4
TW651	14434	46507	0.128	0.0087	0.76	27.3	53.1	115.6	1.94	39.8	<b>4.0</b>	<b>0.2</b>	76.2	213.3
TW651	14435	46510	0.086	0.0105	0.78	24.0	33.8	128.4	1.41	31.9	<b>2.7</b>	<b>0.2</b>	84.2	223.1

<sup>a</sup>F<sub>T</sub> is the α-ejection correction after Farley et al. (1996).

<sup>b</sup>Effective uranium content [U ppm + 0.235\*Th ppm], which can be used as a proxy for radiation damage.

**Note:** Durango apatite reference material was also analysed with these samples (refer to lab nos. 14466, 14467 and 14257 in Table 2).

**Table 4.** Single grain zircon (U-Th)/He analytical data for D- and A-apatite-bearing Cambrian siliciclastic sediments.

Sample	Lab. No.	He#	<sup>4</sup> He (ncc)	Mass (mg)	<sup>*</sup> F <sub>r</sub>	U ppm	Th ppm	Th/U ratio	<sup>b</sup> [eU] ppm	Corrected age (Ma)	Error (±1σ)	Grain length (μm)	Grain half width (μm)	<sup>c</sup> r <sub>s</sub>	<sup>d</sup> Crystal morphology
<b>Authigenic apatite-bearing strata</b>															
TW650	14426	46129	149.064	0.0155	0.85	116.4	65.2	0.56	131.8	<b>559.1</b>	<b>34.7</b>	274.1	69.5	83.2	2T
TW650	14427	46132	128.801	0.0103	0.82	128.8	105.5	0.82	153.6	<b>631.2</b>	<b>39.1</b>	218.6	67.9	77.7	2T
TW650	14428	46135	153.018	0.0141	0.83	137.3	110.2	0.80	163.2	<b>519.1</b>	<b>32.2</b>	284.3	62.8	77.1	2T
TW650	14429	46138	46.662	0.0077	0.78	99.4	73.1	0.74	116.6	<b>412.8</b>	<b>25.6</b>	265.3	45.5	58.3	2T
TW650	14430	46141	165.026	0.0086	0.80	9050.9	295.9	0.03	9120.4	<b>17.3</b>	<b>1.1</b>	243.5	52.7	64.9	2T
TW650	14431	46144	190.250	0.0183	0.82	157.1	93.5	0.60	179.0	<b>457.5</b>	<b>28.4</b>	265.1	60.9	74.3	0T
TW651	14437	46147	321.108	0.0139	0.83	507.4	147.5	0.29	542.0	<b>339.1</b>	<b>21.0</b>	302.6	58.6	73.7	2T
TW651	14438	46150	28.870	0.0077	0.78	53.3	30.9	0.58	60.6	<b>485.1</b>	<b>30.1</b>	260.4	46.3	59.0	2T
TW651	14439	46153	56.155	0.0088	0.80	64.4	48.0	0.75	75.7	<b>653.2</b>	<b>40.5</b>	234.6	55.2	67.1	2T
TW660	18800	62557	59.033	0.0031	0.73	278.3	219.8	0.79	330.0	<b>453.4</b>	<b>28.1</b>	165.2	39.4	47.7	2T
TW660	18801	62560	57.277	0.0040	0.70	359.4	137.1	0.38	391.6	<b>291.4</b>	<b>18.1</b>	248.0	30.9	41.3	1T
TW660	18802	62563	8.615	0.0024	0.70	47.1	4.3	0.09	48.1	<b>583.1</b>	<b>36.1</b>	164.0	33.2	41.4	2T
<b>Detrital apatite-bearing strata</b>															
TW558	14397	46059	83.910	0.0052	0.76	205.7	368.7	1.79	292.3	<b>438.2</b>	<b>27.2</b>	200.5	45.6	55.8	2T
TW558	14398	46062	77.620	0.0050	0.77	213.9	196.9	0.92	260.2	<b>466.9</b>	<b>29.0</b>	183.8	49.1	58.1	2T
TW558	14399	46065	129.691	0.0066	0.76	288.0	292.3	1.01	356.7	<b>436.0</b>	<b>27.0</b>	274.3	40.6	53.0	2T
TW558	14400	46068	104.735	0.0049	0.76	312.3	284.3	0.91	379.1	<b>447.4</b>	<b>27.7</b>	199.7	43.9	54.0	2T
TW558	14401	46071	169.558	0.0108	0.79	193.8	163.6	0.84	232.3	<b>528.3</b>	<b>32.8</b>	327.6	47.4	62.1	2T
TW558	14402	46074	89.185	0.0090	0.79	120.0	219.1	1.83	171.5	<b>458.2</b>	<b>28.4</b>	279.1	48.1	61.5	2T
TW560	14403	46077	129.181	0.0060	0.74	526.5	302.8	0.58	597.6	<b>288.6</b>	<b>17.9</b>	286.2	37.3	49.5	2T
TW560	14404	46080	79.011	0.0069	0.78	137.1	113.4	0.83	163.8	<b>544.5</b>	<b>33.8</b>	250.7	44.8	57.0	2T
TW560	14405	46083	52.619	0.0052	0.75	136.8	139.5	1.02	169.6	<b>473.1</b>	<b>29.3</b>	233.1	39.8	51.0	2T
TW560	14407	46089	43.335	0.0066	0.77	97.3	40.6	0.42	106.9	<b>481.2</b>	<b>29.8</b>	268.8	41.2	53.6	2T
TW560	14408	46092	48.156	0.0040	0.72	150.3	100.2	0.67	173.8	<b>537.9</b>	<b>33.3</b>	230.9	34.6	45.1	2T
TW639	18794	62539	134.302	0.0058	0.76	458.0	212.0	0.46	507.9	<b>360.7</b>	<b>22.4</b>	255.7	39.8	51.7	2T
TW639	18795	62542	93.332	0.0103	0.77	124.4	137.6	1.11	156.7	<b>454.5</b>	<b>28.2</b>	387.8	41.2	55.8	2T
TW639	18796	62545	88.372	0.0087	0.77	154.7	165.3	1.07	193.5	<b>416.4</b>	<b>25.8</b>	288.6	45.9	59.4	2T
TW639	18797	62548	15.356	0.0148	0.85	13.6	2.8	0.20	14.3	<b>561.9</b>	<b>34.8</b>	272.5	67.6	81.3	2T
TW639	18798	62551	131.069	0.0054	0.73	851.7	971.3	1.14	1080.0	<b>180.9</b>	<b>11.2</b>	274.0	36.3	48.1	2T
TW639	18799	62554	138.749	0.0119	0.81	1451.7	918.7	0.63	1667.6	<b>57.0</b>	<b>3.5</b>	257.4	54.3	67.2	1T
TW670	18804	62569	27.848	0.0048	0.75	83.5	56.0	0.67	96.6	<b>469.3</b>	<b>29.1</b>	220.3	40.0	50.8	2T
TW670	18805	62572	103.816	0.0084	0.78	166.8	152.1	0.91	202.5	<b>479.6</b>	<b>29.7</b>	262.2	48.6	61.5	2T
TW670	18806	62575	45.957	0.0064	0.79	94.7	72.3	0.76	111.7	<b>503.1</b>	<b>31.2</b>	185.8	58.5	66.7	2T
TW670	19807	62578	52.272	0.0049	0.78	196.3	124.7	0.64	225.6	<b>375.5</b>	<b>23.3</b>	173.0	52.1	60.0	2T
TW670	18808	62581	87.979	0.0045	0.76	287.3	123.5	0.43	316.3	<b>479.6</b>	<b>29.7</b>	196.3	42.7	52.6	2T
TW670	18809	62584	28.191	0.0043	0.74	90.3	34.5	0.38	98.4	<b>521.2</b>	<b>32.3</b>	195.8	41.2	51.0	2T
TW683	18810	62587	335.341	0.0156	0.83	572.2	352.4	0.62	655.0	<b>263.3</b>	<b>16.3</b>	321.9	59.8	75.6	2T
TW683	18811	62620	68.930	0.0058	0.76	160.0	114.2	0.71	186.8	<b>495.7</b>	<b>30.7</b>	239.0	42.0	53.6	2T
TW683	18812	62623	49.175	0.0062	0.76	116.4	64.5	0.55	131.6	<b>471.0</b>	<b>29.2</b>	258.0	41.1	53.2	2T
TW683	18813	62626	78.002	0.0068	0.75	199.5	142.5	0.71	233.0	<b>392.8</b>	<b>24.4</b>	245.9	41.0	52.7	1T
TW683	18814	62629	74.966	0.0055	0.77	250.7	143.9	0.57	284.6	<b>379.9</b>	<b>23.6</b>	202.1	47.1	57.2	2T
TW683	18815	62632	95.837	0.0081	0.79	154.8	95.5	0.62	177.2	<b>521.5</b>	<b>32.3</b>	202.8	51.3	61.4	1T
<b>Fish Canyon Tuff</b>															
FCT	14410	46098	9.250	0.0074	0.78	324.4	173.0	0.53	365.0	<b>28.2</b>	<b>1.7</b>	248.3	46.9	59.2	2T
FCT	14411	46123	9.774	0.0079	0.79	344.9	167.7	0.49	384.3	<b>26.3</b>	<b>1.6</b>	250.5	48.7	61.2	2T
FCT	14412	46126	5.908	0.0045	0.74	333.7	197.8	0.59	380.2	<b>28.6</b>	<b>1.8</b>	188.2	43.9	53.4	2T
FCT	18689	62536	8.730	0.0060	0.77	366.9	181.4	0.49	409.6	<b>29.3</b>	<b>1.8</b>	236.9	42.8	54.4	2T
FCT	18691	62747	6.499	0.0037	0.75	456.7	226.8	0.50	510.0	<b>28.3</b>	<b>1.8</b>	175.3	41.6	50.4	2T

<sup>\*</sup>F<sub>r</sub> is the α-ejection correction after Farley *et al.* (1996).

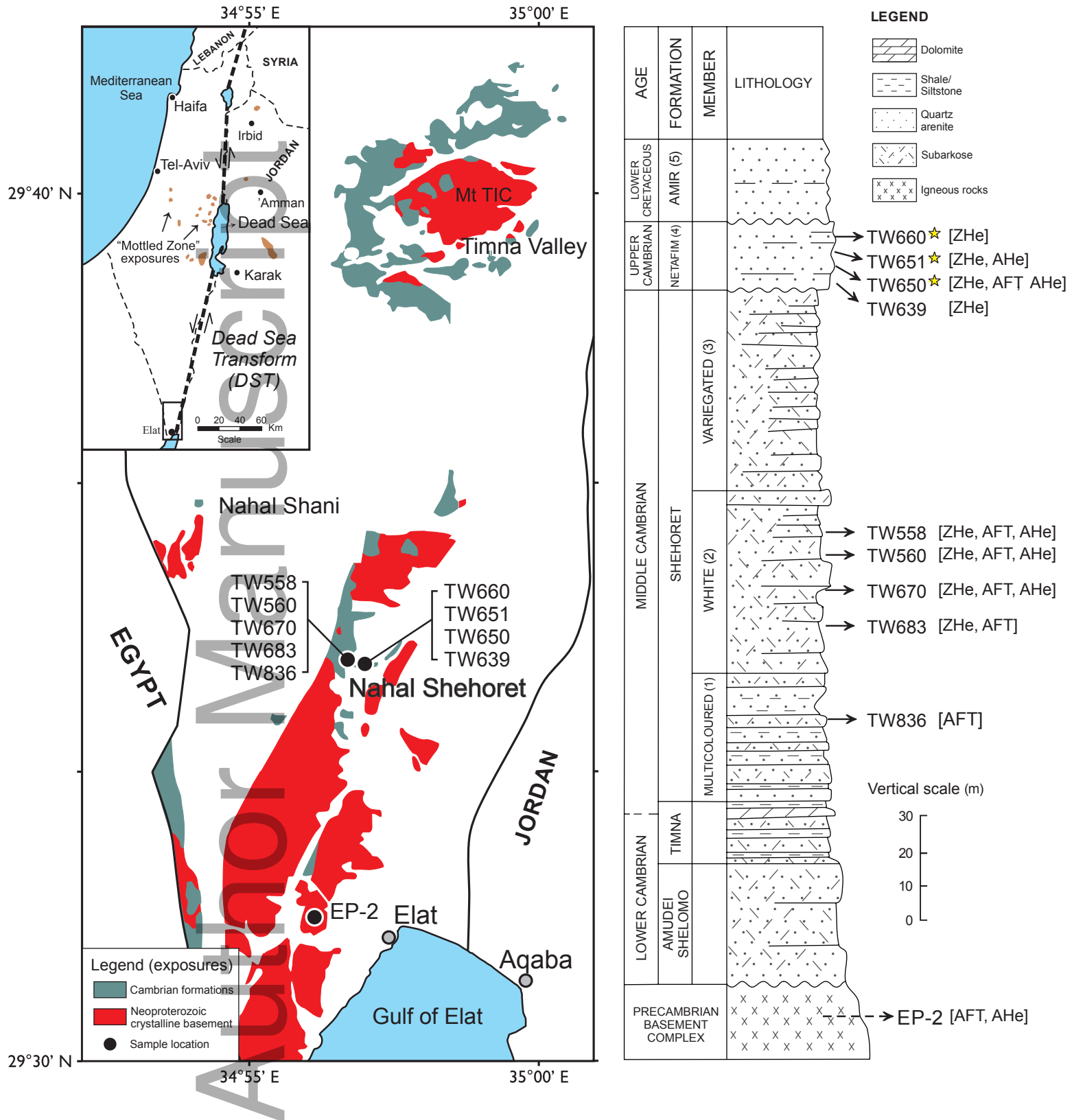
<sup>b</sup>Effective uranium concentration (U ppm+0.235 Th ppm).

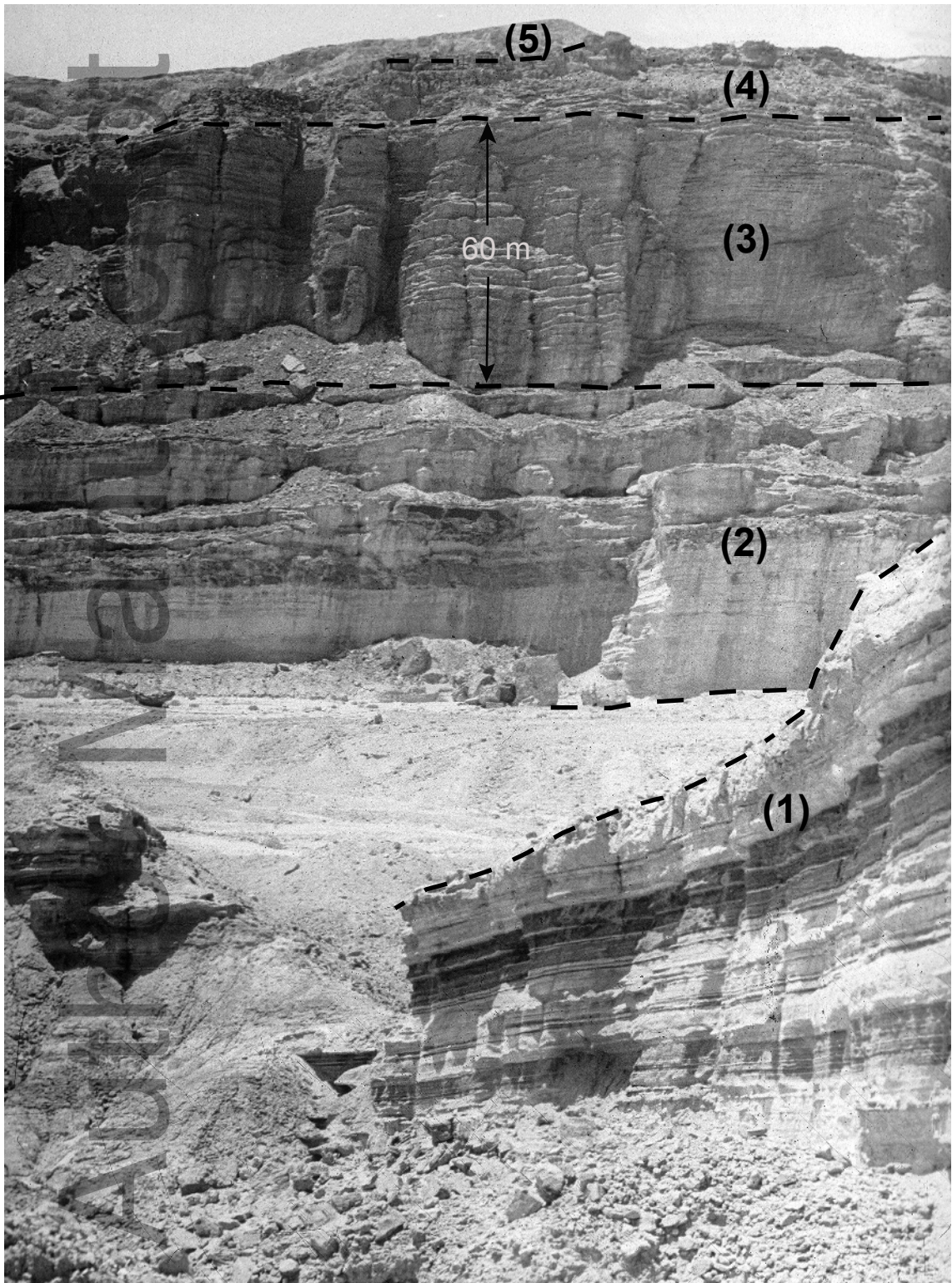
<sup>c</sup>Equivalent spherical radius

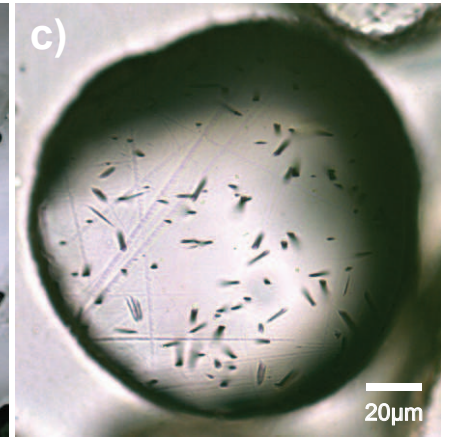
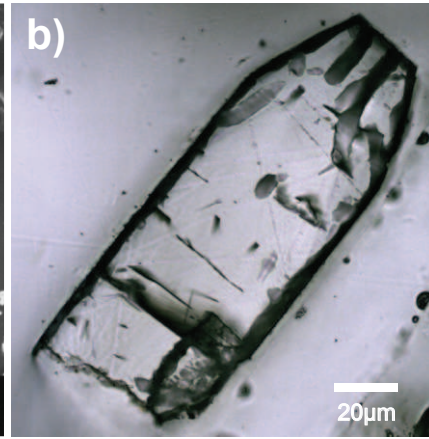
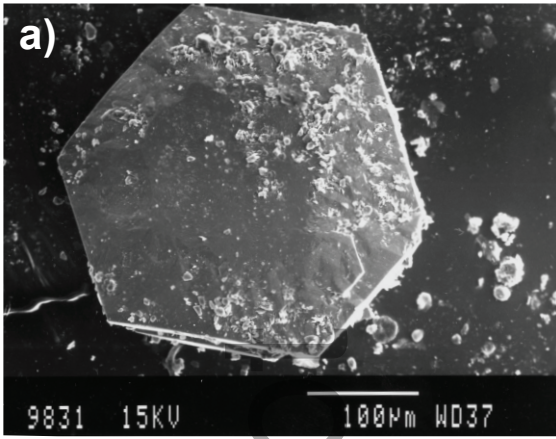
<sup>d</sup>Grain morphology - 0T = no terminations, 1T = one termination, 2T = 2 terminations.

**Notes:** Samples TW651 and TW660 are from different beds of the Netafim Formation at the same locality as sample TW650 in Nahal Shehoret (see Table 1).

Fish Canyon Tuff zircon reference material (28.3±0.4 Ma - Gleadow *et al.*, 2015) was analysed as an internal check with each batch of zircons analysed.







Author Manuscript

